

Vibration in phase-shifting interferometry

Peter J. de Groot

Zygo Corporation, Laurel Brook Road, Middlefield, Connecticut 06455

Received January 14, 1994; revised manuscript received September 15, 1994; accepted September 16, 1994

Unexpected mechanical vibrations can significantly degrade the otherwise high accuracy of phase-shifting interferometry. Fourier analysis of phase-shift algorithms is shown to provide the analytical means of predicting measurement errors as a function of the frequency, the phase, and the amplitude of vibrations. The results of this analysis are concisely represented by a phase-error transfer function, which may be multiplied by the noise spectrum to predict the response of an interferometer to various forms of vibration. Analytical forms for the phase error are derived for several well-known algorithms, and the results are supported by numerical simulations and experiments with an interference microscope.

1. INTRODUCTION

Interferometers are almost invariably equipped with a more-or-less elaborate system to dampen or to isolate vibration. Often the interferometer is constructed of massive machined parts and is placed on a granite slab or an air table. Auxiliary equipment, such as motors and cooling fans, is removed or is kept at a distance. No one is supposed to take a step or to breathe too heavily during the measurement process. If there is a way to observe the interference pattern directly, it is not uncommon to see someone attentively studying the pattern for several minutes at a time, trying to discern small variations attributable to vibration or to air turbulence.

The sensitivity of interferometers to vibration is rooted in the fundamental principles of the instrument. In surface-figure phase-shifting interferometry (PSI) the idea is to measure height variations by means of precise determination of phase angles in an interferogram. Typically, an electronic imaging system stores interferograms for a sequence of reference phases, and then a computer recovers the original wave-front phase by analysis of the variations of intensity as a function of reference-phase shift.^{1,2} The most common method of introducing reference-phase shifts is by sampling interferograms during a time-dependent linear phase ramp, such as can be provided by mechanical translation of the reference surface. The fact that the measurement requires time means that other time-dependent phenomena, such as mechanical vibrations, tend to be convolved into the data.

Phase-measurement errors are most obvious in repeatability tests, when successive measurements are subtracted from one another. An example of a residual error map from a repeatability test in the presence of vibration is shown in Fig. 1. The most obvious problem is the periodic deformation or ripple having a spatial frequency equal to twice that of the interference fringes in the field of view. Ripple is the most common and most recognizable error in PSI.

In addition to vibration, there are several factors that affect PSI measurement precision, resulting in errors in the phase calculation. Many of these factors have been thoroughly studied and reported in the literature and include inadequate precision in the calibration of the

phase ramp,³ nonlinear ramp motion,⁴ detector noise and nonlinearity,⁵ and data corruption by unwanted reflections.^{6,7} Experience has also shown that undesired mechanical motions occurring during the acquisition time period of interference fringe data seriously affect measurement accuracy; however, the current literature on PSI does not adequately address this issue, particularly with regard to means of quantitative analysis of the relative merits of the various PSI algorithms in the presence of vibration. Ideally, this quantitative analysis would characterize the PSI measurement process with a closed-form analytical representation of its sensitivity to various forms of vibrational noise.

The calculation of interferometric phase in PSI involves several steps, usually including at least one division and the evaluation of an inverse trigonometric function. At first glance, the propagation of errors through the various stages of the measurement process seems complicated enough that one must abandon any hope of a reasonable analytical solution to the problem. Traditionally, PSI error analysis has involved a careful modeling of the instrument followed by numerical calculation of phase errors for a series of example situations.⁸ Calculations of this type are increasingly practical now, thanks to computers, but they can still be time consuming, and they do not always reveal those characteristics of PSI algorithms that lead to measurement errors.

In spite of the nonlinear nature of PSI calculations, van Wingerden *et al.*⁹ and Kinnstätter *et al.*¹⁰ have shown that small phase-measurement errors can for the most part be treated as linear perturbations traceable to error sources through relatively simple formulas. Thus a linear approximation should make it possible to derive convenient, closed-form equations capable of predicting phase errors resulting from a wide variety of vibrations.

One way to describe a complex vibration is to decompose it into individual vibration tones, each with its own amplitude, phase, and frequency. In a linear approximation any arbitrary vibration can then be built up from individual tones, each of which makes a contribution to the final phase-measurement error. Of course, this Fourier description of vibration is only useful to us if there is a corresponding Fourier description of PSI. In a recent paper Freischlad and Koliopoulos showed that PSI

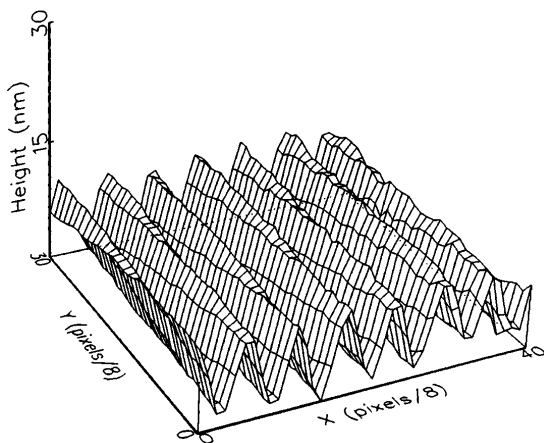


Fig. 1. Experimental phase-error map for an interferometer in the presence of a 1-Hz vibration having an amplitude of approximately one-quarter fringe. There were approximately three fringes in the field of view.

may be considered to be a special form of filtering process in the frequency domain, designed to recover the phase of a specific heterodyne frequency generated by the phase shifting.¹¹ This Fourier approach to PSI builds on some of the original concepts introduced into digital interferometry by Bruning *et al.*¹² and provides an ideal mathematical framework for understanding the propagation of errors.

In this paper the sensitivity of a PSI algorithm will be concisely represented by a phase-error transfer function in the vibrational frequency domain. The derivation of a phase-error transfer function is a worthwhile objective. Not only does it reveal sources of measurement error by explicitly showing the sensitivity of PSI algorithms to particular vibrational frequencies, but the linear approximation makes it possible to predict the effects of continuous, complex noise spectra. The results obtained in this way are general in the sense that one can analyze most commonly known PSI data-acquisition and analysis methods for vibrational sensitivity without rederiving the fundamental formulas. This is shown by a series of example calculations that clearly show the relative merits of different PSI algorithms.

2. INTENSITY DISTORTIONS THAT ARE DUE TO VIBRATION

A good starting point for this analysis is with the hardware and the effects of vibration on the optical image generated by the instrument. Interferometers work by mixing light reflected from the reference surface and the test surfaces, which results in an interference pattern that obeys

$$g(\theta) = Q[1 + V \cos(\theta)], \quad (1)$$

where θ is the interference phase for a particular measurement point on the test surface, V is the fringe visibility or contrast, and Q is an overall constant. The interference phase at each point on the surface is related to the surface height L according to

$$\theta = 4\pi L/\lambda. \quad (2)$$

The accuracy of the surface-profile measurement depends on our ability to determine the phase θ .

In PSI a linear, time-dependent phase shift $\phi(t)$ is introduced over the entire measurement field, usually by means of a mechanical displacement $\delta L(t)$ of the reference surface of the interferometer:

$$\phi(t) = 4\pi \frac{\delta L(t)}{\lambda}. \quad (3)$$

A useful change of variables is facilitated by normalization of the fundamental frequency of the interference pattern to 1, so that

$$t = \phi/2\pi. \quad (4)$$

The interference pattern is now written as

$$g(\theta, \phi) = Q[1 + V \cos(\theta + \phi)]. \quad (5)$$

During a PSI acquisition mechanical vibrations will be added to the linear motion of the phase modulator, resulting in a distorted intensity signal $g'(\theta, \phi)$. Using the phase shift ϕ as the time-variable parameter, we have

$$g'(\theta, \phi) = Q\{1 + V \cos[\phi + \theta - n(\phi)]\}, \quad (6)$$

where $n(\phi)$ is the phase error that is due to vibration at a time $t = \phi/2\pi$. For the purposes of vibration analysis, Eq. (6) is considered to be an exact, nonlinear mathematical model of the interference pattern generated by the instrument. Supplementary sources of error, such as detector nonlinearities, are excluded.

Let us now ponder the effect of intensity errors on the phase measurement. In the presence of vibration it is expected that the phase angle φ measured by the instrument will have an error $\Delta\varphi$ that will be a function of a number of parameters, including the actual phase angle θ :

$$\Delta\varphi(\theta, \dots) = \varphi(\theta, \dots) - \theta. \quad (7)$$

The phase measurement in PSI is normally performed by a quadrature detection that can be written as

$$\varphi(\theta) = \tan^{-1}[s(\theta)/c(\theta)], \quad (8)$$

where we obtain $s(\theta)$ and $c(\theta)$ by fitting ϕ -dependent sine and cosine functions to the intensity variation $g'(\theta, \phi)$. The picture of error propagation that we will keep in mind is as follows. Vibration causes intensity errors, which in turn introduce errors in the numerator $s(\theta)$ and the denominator $c(\theta)$ of the arctangent, which in turn result in an error $\Delta\varphi$ in the final phase φ . This appears to be a good approach to the problem, but we still need a convenient mathematical means of modeling vibrational noise and the resulting intensity distortions.

A useful way to characterize almost any signal is by its frequency content or spectrum. Thus a particular

phase-dependent vibrational noise signal $n(\phi)$ can be represented by a noise spectrum

$$N(\nu) = \text{FT}\{n(\phi)\}, \quad (9)$$

where $\text{FT}\{\}$ is the Fourier transform from phase space to frequency space. The noise can be calculated from its spectrum by use of the inverse Fourier transform:

$$n(\phi) = \text{FT}^{-1}\{N(\nu)\}. \quad (10)$$

The Fourier transform and its inverse are here defined by

$$\text{FT}\{n(\phi)\} = \frac{1}{2\pi} \int_{-\infty}^{\infty} n(\phi) \exp(-i\nu\phi) d\phi, \quad (11)$$

$$\text{FT}^{-1}\{N(\nu)\} = \int_{-\infty}^{\infty} N(\nu) \exp(i\nu\phi) d\nu, \quad (12)$$

where $\phi = 2\pi t$.

To see how vibration with a particular spectrum distorts the intensity data acquired during the measurement process, first expand the exact equation, Eq. (6), for the intensity:

$$g'(\theta, \phi) = Q + QV\{\cos[n(\phi)]\cos(\phi + \theta) + \sin[n(\phi)] \times \sin(\phi + \theta)\}. \quad (13)$$

For small-amplitude vibrations this result simplifies to

$$g'(\theta, \phi) \approx g(\theta, \phi) + \Delta g(\theta, \phi), \quad (14)$$

where

$$\Delta g(\theta, \phi) = QVn(\phi)\sin(\phi + \theta). \quad (15)$$

From now on the small-amplitude, linear approximation is implicit. The function $\Delta g(\theta, \phi)$ is the contribution of each vibrational frequency ν to the distortion of the normal intensity variation expected during the PSI data-acquisition process.

The Fourier transform of relation (14), with ϕ as the time-dependent variable, generates a spectrum of values as a function of frequencies $\hat{\nu}$ in the intensity data:

$$\Delta G(\theta, \hat{\nu}) = \text{FT}\{n(\phi)\sin(\theta + \phi)\}QV. \quad (16)$$

By the convolution theorem,

$$\Delta G(\theta, \hat{\nu}) = QVN(\hat{\nu}) \otimes (i/2)[\delta(\hat{\nu} - 1)\exp(i\theta) - \delta(\hat{\nu} + 1) \times \exp(-i\theta)], \quad (17)$$

where $\delta(a - b)$ is the Dirac delta function. Evaluating the convolution, we obtain

$$\Delta G(\theta, \hat{\nu}) = QV(i/2)[N(\hat{\nu} - 1)\exp(i\theta) - N(\hat{\nu} + 1) \times \exp(-i\theta)]. \quad (18)$$

This result shows that a vibration of frequency ν generates an intensity distortion composed of two frequencies $\hat{\nu} = \nu + 1$ and $\hat{\nu} = \nu - 1$ of equal amplitude, with essentially the same dependence on θ for all frequencies. Thus the expected errors that are due to small-amplitude vibrations will have essentially the same periodic behavior, regardless of the nature of the noise. Typically, the phase-dependent error manifests itself either as an ad-

ditive constant or as a ripple in the data at twice the frequency of the normal interference variation.

3. PROPAGATION OF ERRORS

Equation (18) is an analytical formula for the spectrum of intensity distortions generated by small-amplitude vibrations. The next step is to see how these intensity errors propagate through the PSI algorithm. In the following analysis the general approach and some of the mathematical steps build on the Freischlad-Koliopoulos¹¹ and Larkin-Oreb¹³ research. The principal difference is the form of intensity distortion, which for this paper is related to a spectrum of vibrational tones.

For small-amplitude vibrations the phase error $\Delta\phi$ resulting from vibrations can be meaningfully decomposed into a spectrum of contributions arising from each of the individual frequency components of the noise source. The relationship between the noise spectrum and the spectrum of phase errors can therefore be put into the form

$$\Delta\phi(\theta) = \int_{-\infty}^{\infty} N(\nu)P(\nu, \theta)d\nu, \quad (19)$$

in which the phase-error transfer function $P(\nu, \theta)$ describes the sensitivity of PSI to the various frequency components of the noise signal.

The phase-error transfer function $P(\nu, \theta)$ in Eq. (19) is a compact description of the response to vibration, including the data-sampling characteristics of the PSI algorithm as well as other linear factors relating to the instrument, such as the video camera frame rate and integration time. To derive a formula for this function in terms of recognizable PSI parameters we return to the quadrature formula function introduced in Eq. (8):

$$\phi(\theta) = \tan^{-1}[s(\theta)/c(\theta)]. \quad (20)$$

The quantities $s(\theta)$ and $c(\theta)$ may be expressed as correlations of the noise-corrupted intensity function $g'(\theta, \phi)$ with two discrete sampling functions $f_s(\phi)$ and $f_c(\phi)$, evaluated at $t = 0$:

$$s(\theta) = \int_{-\infty}^{\infty} f_s(\phi)g'(\theta, \phi)d\phi, \quad (21)$$

$$c(\theta) = \int_{-\infty}^{\infty} f_c(\phi)g'(\theta, \phi)d\phi.$$

Although the ratio of $s(\theta)$ to $c(\theta)$ is a measure of the arctangent of the phase, the actual values of $s(\theta)$ and $c(\theta)$ will obviously depend on scaling factors such as the intensity Q , the fringe visibility V , and the weights given to the sampling functions $f_s(\phi)$ and $f_c(\phi)$. The ratio should be independent of these scaling factors when the sampling functions are properly constructed. Thus, in the limit of zero vibrational noise, we should be able to write

$$s(\theta) \approx QVq \sin(\theta), \quad (22)$$

$$c(\theta) \approx QVq \cos(\theta),$$

where, by correlation with perfect sine and cosine

functions,

$$q = \int_{-\infty}^{\infty} f_S(\phi) \sin(-\phi) d\phi = \int_{-\infty}^{\infty} f_C(\phi) \cos(\phi) d\phi. \quad (23)$$

We are now in a position to estimate the phase errors $\Delta\varphi$ for small errors $\Delta s(\theta)$ and $\Delta c(\theta)$:

$$\Delta\varphi(\theta) \approx \left[\Delta s(\theta) \frac{d\varphi}{ds} + \Delta c(\theta) \frac{d\varphi}{dc} \right]. \quad (24)$$

Evaluating the derivatives for $\varphi = \theta$, we obtain

$$\Delta\varphi(\theta) \approx \frac{1}{QVq} [\Delta s(\theta) \cos(\theta) - \Delta c(\theta) \sin(\theta)]. \quad (25)$$

Recall the linear approximation [Eq. (13)] for intensity distortions; the errors that are due to vibrations are

$$\begin{aligned} \Delta s(\theta) &= \int_{-\infty}^{\infty} f_S(\phi) \Delta g(\theta, \phi) d\phi, \\ \Delta c(\theta) &= \int_{-\infty}^{\infty} f_C(\phi) \Delta g(\theta, \phi) d\phi. \end{aligned} \quad (26)$$

The integrals can be transformed to the frequency domain by use of Parseval's theorem¹⁴:

$$\begin{aligned} \Delta s(\theta) &= q \int_{-\infty}^{\infty} F_S^*(\hat{\nu}) \Delta G(\theta, \hat{\nu}) d\hat{\nu}, \\ \Delta c(\theta) &= q \int_{-\infty}^{\infty} F_C^*(\hat{\nu}) \Delta G(\theta, \hat{\nu}) d\hat{\nu}, \end{aligned} \quad (27)$$

where $F_S(\hat{\nu})$ and $F_C(\hat{\nu})$ are the complex Fourier transforms of the real functions $f_S(\phi)$ and $f_C(\phi)$, normalized by the common weighting factor $q/2\pi$.

Relation (25) for the phase error $\Delta\varphi(\theta)$ can now be written in terms of frequency spectra:

$$\Delta\varphi(\theta) = \frac{1}{QV} \int_{-\infty}^{\infty} [F_S^*(\hat{\nu}) \cos(\theta) - F_C^*(\hat{\nu}) \sin(\theta)] \Delta G(\theta, \hat{\nu}) d\hat{\nu}. \quad (28)$$

By insertion of the previously derived Eq. (18) for the spectrum of intensity errors $\Delta G(\theta, \hat{\nu})$, this result becomes

$$\begin{aligned} \Delta\varphi(\theta) &= \frac{i}{2} \int_{-\infty}^{\infty} N(\hat{\nu} - 1) [F_S^*(\hat{\nu}) \cos(\theta) - F_C^*(\hat{\nu}) \sin(\theta)] \\ &\quad \times \exp(+i\theta) d\hat{\nu} - \frac{i}{2} \int_{-\infty}^{\infty} N(\hat{\nu} + 1) [F_S^*(\hat{\nu}) \cos(\theta) \\ &\quad - F_C^*(\hat{\nu}) \sin(\theta)] \exp(-i\theta) d\hat{\nu}. \end{aligned} \quad (29)$$

By a simple change of variable, the two integrals can be combined into one integral over the range of vibrational frequencies present in the noise spectrum $N(\nu)$:

$$\begin{aligned} \Delta\varphi(\theta) &= \frac{i}{2} \int_{-\infty}^{\infty} N(\nu) \{ [F_S^*(\nu + 1) \cos(\theta) - F_C^*(\nu + 1) \sin(\theta)] \\ &\quad \times \exp(+i\theta) - [F_S^*(\nu - 1) \cos(\theta) - F_C^*(\nu - 1) \\ &\quad \times \sin(\theta)] \exp(-i\theta) \} d\nu. \end{aligned} \quad (30)$$

The following trigonometric identities are useful for collecting terms in the integrand:

$$\begin{aligned} \exp(\pm i\theta) &= \cos(\theta) \pm i \sin(\theta), \\ 2 \sin(\theta) \cos(\theta) &= \sin(2\theta), \\ 2 \cos^2(\theta) &= 1 + \cos(2\theta), \\ 2 \sin^2(\theta) &= 1 - \cos(2\theta). \end{aligned} \quad (31)$$

After terms are gathered together the phase error is in the desired form [cf. Eq. (19)]:

$$\Delta\varphi(\theta) = \int_{-\infty}^{\infty} N(\nu) P(\nu, \theta) d\nu, \quad (32)$$

where the phase-error transfer function $P(\nu, \theta)$ is

$$\begin{aligned} P(\nu, \theta) &= P_0(\nu) + P_1(\nu) \cos(2\theta) + P_2(\nu) \sin(2\theta), \\ P_0(\nu) &= \frac{1}{4} \{ F_C^*(\nu + 1) + F_C^*(\nu - 1) \\ &\quad + i [F_S^*(\nu + 1) - F_S^*(\nu - 1)] \}, \\ P_1(\nu) &= \frac{1}{4} \{ -F_C^*(\nu + 1) - F_C^*(\nu - 1) \\ &\quad + i [F_S^*(\nu + 1) - F_S^*(\nu - 1)] \}, \\ P_2(\nu) &= \frac{1}{4} \{ -F_S^*(\nu + 1) - F_S^*(\nu - 1) \\ &\quad - i [F_C^*(\nu + 1) - F_C^*(\nu - 1)] \}. \end{aligned} \quad (33)$$

The fundamental objective of deriving a general formula for the propagation of errors that are due to small-amplitude vibrations is now complete. To quantify the phase error for a particular vibrational noise spectrum, the Fourier transforms of the numerator and the denominator of a PSI algorithm are inserted into Eqs. (33) to calculate a phase-error transfer function $P(\nu, \theta)$ characteristic of that algorithm. The transfer function $P(\nu, \theta)$ can then be used, with Eq. (32), to calculate the net phase error $\Delta\varphi(\theta)$ that is due to vibration.

4. ADDITIONAL EFFECTS

Because the analytical method is founded on Fourier analysis, additional frequency-dependent effects are easily included. For example, in calculating the filter spectra $F_S(\hat{\nu})$ and $F_C(\hat{\nu})$ it is important to include details of the intensity-detection mechanism, which can have a profound influence on the frequency response of the PSI algorithm. The intensity measurement requires time for accumulation of light for a strong signal, and during this time period the intensity data are being integrated. The effect of this integration on the mathematical model is that the PSI filter functions $f_S(\phi)$, $f_C(\phi)$ are in fact the results of convolutions of discrete sampling functions $h_S(\phi)$ and $h_C(\phi)$ characteristic of the PSI algorithm with a detector function $b(\phi)$ related to the instrument hardware:

$$\begin{aligned} f_S(\phi) &= h_S(\phi) \otimes b(\phi), \\ f_C(\phi) &= h_C(\phi) \otimes b(\phi). \end{aligned} \quad (34)$$

These convolutions are conveniently represented in the frequency domain by a simple multiplication of function spectra:

$$F_S(\hat{\nu}) = H_S(\hat{\nu})B(\hat{\nu}), \quad (35)$$

where $H_S(\hat{\nu})$ is normalized by $q/2\pi$ and $B(\hat{\nu})$ is normalized to 1 for a data-acquisition frequency $\hat{\nu} = 1$. The detector function $b(\phi)$ typically is of the form

$$b(\phi) = \begin{cases} 1 & |\phi| \leq \beta/2 \\ 0 & |\phi| > \beta/2 \end{cases}, \quad (36)$$

where β is the dwell time of the detector, expressed in terms of the phase-shift variation $\phi = 2\pi t$. For this case, commonly known as an integrating bucket, we have

$$B(\hat{\nu}) = \frac{\int_{-\infty}^{\infty} b(\phi)\exp(-i\phi\hat{\nu})d\phi}{\int_{-\infty}^{\infty} b(\phi)\exp(-i\phi)d\phi}, \quad (37)$$

$$B(\hat{\nu}) = \frac{\sin(\hat{\nu}\beta/2)}{\hat{\nu}\sin(\hat{\nu}\beta/2)}. \quad (38)$$

To keep the final equations for the examples given in Section 4 reasonably compact, it is convenient to define

$$B_{\nu\pm 1} = B(\nu \pm 1). \quad (39)$$

As a final note to this section regarding the general mathematical method, it is useful to note that the typical PSI algorithm may be described mathematically as a weighted, linear sum of intensity samples at discrete phase intervals ϕ_j :

$$\begin{aligned} h_S(\phi) &= \sum_j h_{S,j}\delta(\phi - \phi_j), \\ h_C(\phi) &= \sum_j h_{C,j}\delta(\phi - \phi_j). \end{aligned} \quad (40)$$

These functions are devised in such a way that, for uncorrupted intensity data sampled instantaneously at the indicated phase intervals,

$$\theta = \tan^{-1} \left[\frac{\sum_j h_{S,j}g(\theta, \phi_j)}{\sum_j h_{C,j}g(\theta, \phi_j)} \right]. \quad (41)$$

The Fourier transforms of these discrete sampling functions normalized to $q/2\pi$ are

$$\begin{aligned} H_S(\hat{\nu}) &= \frac{1}{q} \sum_j h_{S,j} \exp(-i\phi_j\hat{\nu}), \\ H_C(\hat{\nu}) &= \frac{1}{q} \sum_j h_{C,j} \exp(-i\phi_j\hat{\nu}), \end{aligned} \quad (42)$$

where, from Eq. (23),

$$q = \sum_j h_{S,j} \sin(-\phi_j) = \sum_j h_{C,j} \cos(\phi_j). \quad (43)$$

These observations are useful in the examples given below.

5. EXAMPLE ALGORITHMS

A. Three-Bucket Algorithm

The three-bucket algorithm represents the minimalist approach to PSI. Mathematically, we require at least three different intensity samples to determine the interferometric phase independence of fringe contrast and overall intensity. The three-bucket technique presents advantages that are important enough, in terms of data-acquisition speed, processing time, and storage requirements, to be included here as an example.

According to one well-known version of the three-bucket algorithm,¹⁵ the interferometric phase calculation is represented by the idealized equation

$$\theta = \tan^{-1} \left(\frac{g_3 - g_2}{g_1 - g_2} \right), \quad (44)$$

where

$$g_j = g[\theta, (j\pi/2 - \pi/4)] \quad (45)$$

and the bucket length $\beta = \pi/2$. The data-sampling functions for the three-bucket algorithm are

$$\begin{aligned} h_S(\phi) &= \delta(\phi - 5\pi/4) - \delta(\phi - 3\pi/4), \\ h_C(\phi) &= \delta(\phi - \pi/4) - \delta(\phi - 3\pi/4). \end{aligned} \quad (46)$$

Following Eqs. (42), we find that the corresponding normalized spectra for these sampling functions work out to be

$$\begin{aligned} H_S(\hat{\nu}) &= -i\sqrt{2} \sin(\pi\hat{\nu}/4)\exp(-i\pi\hat{\nu}), \\ H_C(\hat{\nu}) &= i\sqrt{2} \sin(\pi\hat{\nu}/4)\exp(-i\pi\hat{\nu}/2). \end{aligned} \quad (47)$$

The coefficients of the phase-error transfer function $P(\nu, \theta)$ for the three-bucket algorithm are

$$\begin{aligned} P_0(\nu) &= \frac{i \exp(i3\nu\pi/4)\cos(\nu\pi/4)}{2} (B_{\nu+1} + B_{\nu-1}) \\ &\quad \times \cos(\nu\pi/4) + (B_{\nu+1} - B_{\nu-1})\sin(\nu\pi/4), \\ P_1(\nu) &= \frac{i \exp(i3\nu\pi/4)\cos(\nu\pi/4)}{2} (B_{\nu+1} + B_{\nu-1}) \\ &\quad \times \cos(\nu\pi/4) + (B_{\nu+1} - B_{\nu-1})\sin(\nu\pi/4), \\ P_2(\nu) &= -\frac{\exp(i3\nu\pi/4)\sin(\nu\pi/4)}{2} (B_{\nu+1} - B_{\nu-1}) \\ &\quad \times \cos(\nu\pi/4) + (B_{\nu+1} + B_{\nu-1})\sin(\nu\pi/4). \end{aligned} \quad (48)$$

B. Four-Bucket Algorithm

In terms of overall performance, the four-bucket algorithm is a significant improvement over the three-bucket algorithm, at the cost of slightly greater memory requirements.¹⁶ One form of the four-bucket algorithm is represented by the idealized equation

$$\theta = \tan^{-1} \left(\frac{g_2 - g_4}{g_3 - g_1} \right), \quad (49)$$

where

$$g_j = g[\theta, (j\pi/2 - \pi)] \quad (50)$$

and the bucket length $\beta = \pi/2$. The corresponding normalized spectra for the sampling functions are

$$\begin{aligned} H_S(\hat{\nu}) &= i \sin(\pi\hat{\nu}/2), \\ H_C(\hat{\nu}) &= \sin^2(\pi\hat{\nu}/2) - (i/2)\sin(\pi\hat{\nu}). \end{aligned} \quad (51)$$

The coefficients of the phase-error transfer function $P(\nu, \theta)$ for the four-bucket algorithm are

$$\begin{aligned} P_0(\nu) &= \frac{(B_{\nu+1} + B_{\nu-1})}{2} \left[\cos(\nu\pi/2)\cos^2(\nu\pi/4) \right. \\ &\quad \left. - \frac{i}{4} \sin(\nu\pi) \right], \\ P_1(\nu) &= \frac{(B_{\nu+1} + B_{\nu-1})}{2} \left[\cos(\nu\pi/2)\sin^2(\nu\pi/4) \right. \\ &\quad \left. + \frac{i}{4} \sin(\nu\pi) \right], \\ P_2(\nu) &= \frac{(B_{\nu+1} - B_{\nu-1})}{2} \left[\cos(\nu\pi/2)\sin^2(\nu\pi/4) \right. \\ &\quad \left. + \frac{i}{4} \sin(\nu\pi) \right]. \end{aligned} \quad (52)$$

C. Schwider–Hariharan Algorithm

A PSI algorithm based on five intensity samples was introduced by Schwider *et al.*¹⁷ and was later popularized by Hariharan *et al.*¹⁸ and by Greivenkamp and Bruning.¹⁹ One of the most attractive features of the method is its relative insensitivity to variations in the phase increment in comparison with traditional three- and four-bucket algorithms. This advantage is important for large-aperture interferometry because of the difficulty in precisely calibrating the piezoelectric transducer (PZT) pushers that perform the phase stepping and because of complications that arise with fast spherical cavities.

The five-bucket algorithm may be represented by the idealized equation

$$\theta = \tan^{-1} \left[\frac{2(g_2 - g_4)}{2g_3 - g_1 - g_5} \right], \quad (53)$$

where

$$g_j = g[\theta, (j\pi/2 - 3\pi/2)] \quad (54)$$

and the bucket length $\beta = \pi/2$. The corresponding normalized spectra for the sampling functions are

$$\begin{aligned} H_S(\hat{\nu}) &= i \sin(\pi\hat{\nu}/2), \\ H_C(\hat{\nu}) &= \sin^2(\pi\hat{\nu}/2). \end{aligned} \quad (55)$$

The coefficients of the phase-error transfer function $P(\nu, \theta)$ for the five-bucket algorithm are

$$\begin{aligned} P_0(\nu) &= \frac{(B_{\nu+1} + B_{\nu-1})}{2} \cos(\nu\pi/2)\cos^2(\nu\pi/4), \\ P_1(\nu) &= \frac{(B_{\nu+1} + B_{\nu-1})}{2} \cos(\nu\pi/2)\sin^2(\nu\pi/4), \\ P_2(\nu) &= i \frac{(B_{\nu+1} - B_{\nu-1})}{2} \cos(\nu\pi/2)\sin^2(\nu\pi/4). \end{aligned} \quad (56)$$

D. Seven-Bucket Algorithm

One way of further enhancing the performance of PSI is to use windowing concepts that are very well known in signal-processing disciplines.²⁰ The larger the data set, the more accurately the data set can be windowed. Thus it is possible to increase the insensitivity to variations in the phase increment by using more than five buckets.

A recently introduced seven-bucket algorithm²¹ based on the von Hann window is represented by the idealized equation

$$\theta = \tan^{-1} \left[\frac{7(g_2 - g_4) - (g_0 - g_6)}{8g_3 - 4(g_1 + g_5)} \right], \quad (57)$$

where

$$g_j = g[\theta, (j\pi/2 - 3\pi/2)] \quad (58)$$

and the bucket length $\beta = \pi/2$. The corresponding normalized spectra for the sampling functions are

$$\begin{aligned} H_S(\hat{\nu}) &= i \sin(\pi\hat{\nu}/2) - (i/8)[\sin(3\pi\hat{\nu}/2) + \sin(\pi\hat{\nu}/2)], \\ H_C(\hat{\nu}) &= \sin^2(\pi\hat{\nu}/2). \end{aligned} \quad (59)$$

The coefficients of the phase-error transfer function $P(\nu, \theta)$ for the seven-bucket algorithm are

$$\begin{aligned} P_0(\nu) &= (B_{\nu+1} + B_{\nu-1}) \left[\frac{\cos(\nu\pi/2)\cos^2(\nu\pi/4)}{2} \right. \\ &\quad \left. + \frac{\cos(3\nu\pi/2) - \cos(\nu\pi/2)}{32} \right], \\ P_1(\nu) &= (B_{\nu+1} + B_{\nu-1}) \left[\frac{\cos(\nu\pi/2)\sin^2(\nu\pi/4)}{2} \right. \\ &\quad \left. + \frac{\cos(3\nu\pi/2) - \cos(\nu\pi/2)}{32} \right], \\ P_2(\nu) &= i(B_{\nu+1} - B_{\nu-1}) \left[\frac{\cos(\nu\pi/2)\sin^2(\nu\pi/4)}{2} \right. \\ &\quad \left. + \frac{\cos(3\nu\pi/2) - \cos(\nu\pi/2)}{32} \right]. \end{aligned} \quad (60)$$

E. Larkin–Oreb Algorithm

From the functional form of the sampling-function spectra $H_S(\hat{\nu})$ and $H_C(\hat{\nu})$ given in the previous four examples it may be inferred that a common feature of many PSI algorithms based on $\pi/2$ phase shifts is zero sensitivity to even-order ($\hat{\nu} = 2, 4, 6, 8 \dots$) harmonic distortions of

the intensity spectrum. However, these algorithms also have a high sensitivity to odd-harmonic distortions. Recently, Larkin and Oreb proposed a new algorithm that, without sacrificing insensitivity to even-order harmonics, is specifically designed to be insensitive to intensity distortions having a frequency of $\hat{\nu} = 3$.²² The algorithm has excellent performance when used in projection moiré interferometry.

The Larkin–Oreb algorithm is represented by the idealized equation

$$\theta = \tan^{-1} \left\{ \sqrt{3} \left[\frac{g_2 + g_3 - g_5 - g_6 + (g_7 - g_1)/3}{-g_1 - g_2 + g_3 + 2g_4 + g_5 - g_6 - g_7} \right] \right\}, \quad (61)$$

where

$$g_j = g[\theta, (j\pi/3 - 4\pi/3)] \quad (62)$$

and the bucket length $\beta = \pi/3$. The corresponding normalized spectra for the sampling functions are

$$\begin{aligned} H_S(\hat{\nu}) &= \frac{\sqrt{3}}{3} i \left[\frac{1}{3} \sin(\pi\hat{\nu}) - \sin(\pi\hat{\nu}/3) - \sin(\pi 2\hat{\nu}/3) \right], \\ H_C(\hat{\nu}) &= \frac{1}{3} \left[-\cos(\pi\hat{\nu}) - \cos(\pi 2\hat{\nu}/3) + 1 + \cos(\pi\hat{\nu}/3) \right]. \end{aligned} \quad (63)$$

The coefficients of the phase-error transfer function $P(\nu, \theta)$ for the Larkin–Oreb algorithm are

$$\begin{aligned} P_0(\nu) &= \frac{(B_{\nu+1} + B_{\nu-1})}{6} [\cos(\nu\pi/3) + \cos(\nu 2\pi/3) \\ &\quad + \cos^2(\nu\pi/2)] + \frac{\sqrt{3}(B_{\nu+1} - B_{\nu-1})}{36} \sin(\nu\pi), \\ P_1(\nu) &= \frac{(B_{\nu+1} + B_{\nu-1})}{12} [\cos(\nu\pi/3) + \cos(\nu 2\pi/3) \\ &\quad - 2 \cos^2(\nu\pi/2)] + \frac{\sqrt{3}(B_{\nu+1} - B_{\nu-1})}{36} \\ &\quad \times [\sin(\nu\pi) - 3 \sin(\nu 2\pi/3) + 3 \sin(\nu\pi/3)], \\ P_2(\nu) &= i \frac{(B_{\nu+1} - B_{\nu-1})}{12} [\cos(\nu\pi/3) + \cos(\nu 2\pi/3) \\ &\quad - 2 \cos^2(\nu\pi/2)] + \frac{i\sqrt{3}(B_{\nu+1} + B_{\nu-1})}{36} \\ &\quad \times [\sin(\nu\pi) - 3 \sin(\nu 2\pi/3) + 3 \sin(\nu\pi/3)]. \end{aligned} \quad (64)$$

6. NUMERICAL SIMULATION

Now that the phase-error transfer functions $P(\nu, \theta)$ for a few common PSI algorithms have been calculated, it is straightforward to predict the response to various types of vibration. The small-amplitude, linear approach to vibrational noise contributions to PSI measurement errors can be used for any noise source that can be represented by a spectrum of complex coefficients $N(\nu)$.

An example of a vibrational noise is provided by the computer-generated signal $n(\phi)$ shown in Fig. 2, which

corresponds to the superposition of three vibrations of different frequency, phase, and amplitude. One can use artificial signals of this kind to verify numerically the validity of the equations derived by the linear approach. To this end, the vibration shown in Fig. 2 is added to a pure sinusoidal signal, and the resulting error is calculated numerically by use of the Schwider–Hariharan algorithm as it appears in Eq. (53). The numerical calculation takes into account the effect of the integrating buckets by averaging ten values for each intensity sample g_j over a phase range of $\pm\pi/4$ in the neighborhood of each sample phase ϕ . The resulting phase error $\Delta\phi(\theta)$ for the numerical simulation is plotted in Fig. 3. Also shown in Fig. 3 is the result of the analytical approach, based on the vibrational noise spectrum and the phase-error transfer function $P(\nu, \theta)$. The close correspondence to the numerical calculation is typical for phase errors below 1 rad. Simulations of this type confirm the usefulness of the linear approximation for complex vibrations.

7. VIBRATIONS OF RANDOM PHASE

In many practical situations we know something about the frequency content of vibrational noise in a given en-

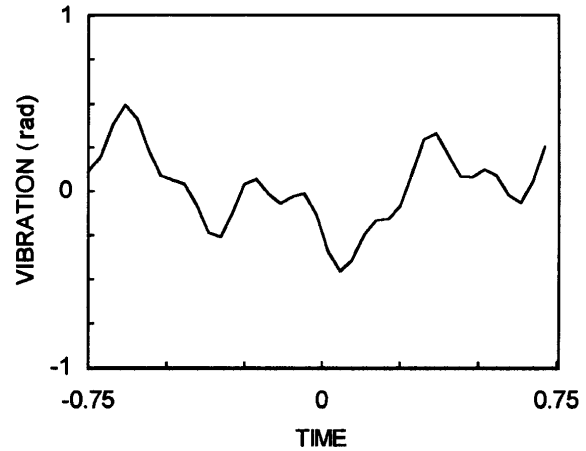


Fig. 2. Vibrational noise signal used for a numerical simulation of phase error.

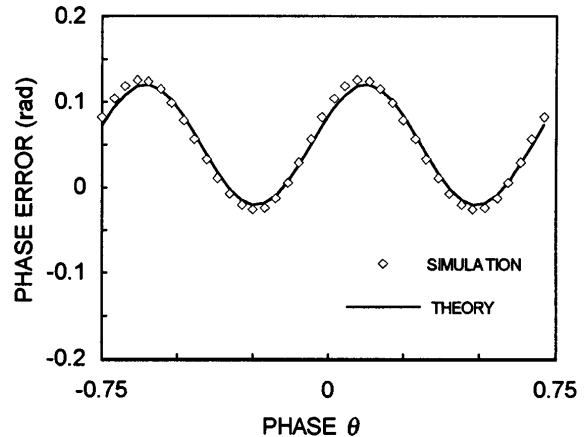


Fig. 3. Comparison of a numerical simulation of phase error with the theoretical predictions based on the phase-error transfer function $P(\nu, \theta)$. The close correspondence is typical of phase errors of less than 1 rad.

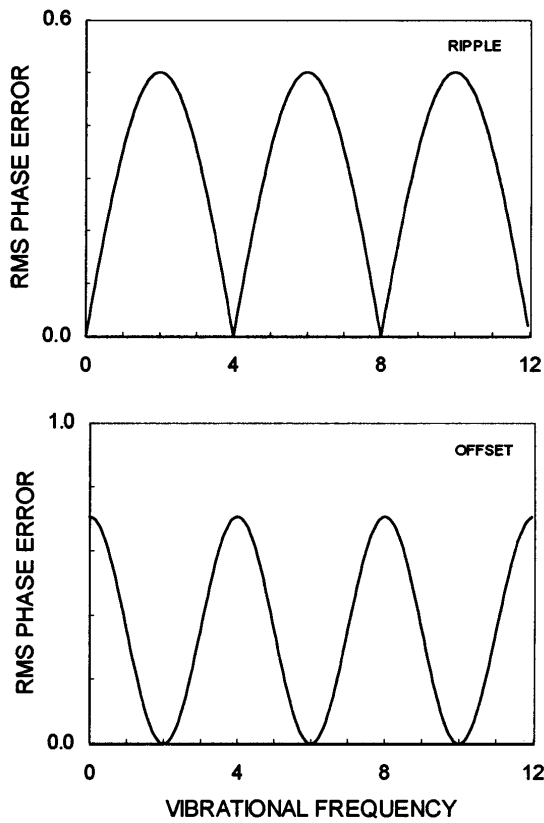


Fig. 4. Predicted rms phase-measurement errors for the three-bucket algorithm with instantaneous phase sampling ($\beta = 0$). The vertical scale is normalized to the vibrational amplitude, and the horizontal scale is normalized to the phase-shift rate, in units of 2π rad/unit time. The upper graph refers to the errors $E_{\nu}^{(r)}$ periodic in the phase angle, whereas the lower graph refers to the constant offset error $E_{\nu}^{(c)}$.

vironment, but the phase information is unknown or random. In this case it is preferable to express the phase error in terms of a root-mean square (rms) expectation. This is the number that we would expect to obtain experimentally after calculating the rms phase error for a large number of measurements in the presence of a random vibration. The mathematical approach proposed here is to calculate the exact phase error as a function of frequency and then find the mean-square error by integrating over all the phase angles.

The phase-averaging approach is most meaningful for single vibrational tones or for simple vibrations having a limited number of spectral components that may be considered to be completely uncorrelated in phase. For the simplest example of a single vibrational frequency ν , the noise spectrum $N(\nu')$ can be written as

$$N(\nu') = \frac{1}{2} A_{\nu} [\exp(i\alpha)\delta(\nu' - \nu) + \exp(-i\alpha)\delta(\nu' + \nu)]. \quad (65)$$

The goal of this section, then, is to determine the expected rms phase-measurement error resulting from a vibrational tone of amplitude A_{ν} , assuming a random phase α .

In the linear approximation, as we have seen, there are essentially two kinds of phase error. The first is in-

dependent of the phase angle θ , and the other is periodic in phase, at the rate of two times the fringe frequency. Thus, for a given vibrational amplitude A_{ν} in the noise spectrum, we can define two rms errors, $E_{\nu}^{(c)}$ and $E_{\nu}^{(r)}$, with the second of these referring to the θ -dependent ripple. Let us also define two corresponding phase-averaged functions, $C(\nu)$ and $R(\nu)$, so that

$$E_{\nu}^{(c)} = A_{\nu} C(\nu), \quad (66)$$

$$E_{\nu}^{(r)} = A_{\nu} R(\nu). \quad (67)$$

From Eq. (32) and the Hermitian properties of $P(\nu, \theta)$, one can infer that the mean-square phase errors over all angles α and θ are

$$[E_{\nu}^{(c)}]^2 = \frac{1}{4\pi^2} \int_{-\pi}^{\pi} \int_{-\pi}^{\pi} \text{Re}\{A_{\nu} P_0(\nu, \theta) \exp(i\alpha)\}^2 d\theta d\alpha. \quad (68)$$

$$[E_{\nu}^{(r)}]^2 = \frac{1}{4\pi^2} \int_{-\pi}^{\pi} \int_{-\pi}^{\pi} \text{Re}\{A_{\nu} [P(\nu, \theta) - P_0(\nu, \theta)] \times \exp(i\alpha)\}^2 d\theta d\alpha. \quad (69)$$

The phase-averaged functions $C(\nu)$ and $R(\nu)$ are therefore

$$C(\nu)^2 = \frac{1}{4\pi^2} \int_{-\pi}^{\pi} \int_{-\pi}^{\pi} c(\nu, \alpha, \theta)^2 d\theta d\alpha, \quad (70)$$

$$R(\nu)^2 = \frac{1}{4\pi^2} \int_{-\pi}^{\pi} \int_{-\pi}^{\pi} r(\nu, \alpha, \theta)^2 d\theta d\alpha, \quad (71)$$

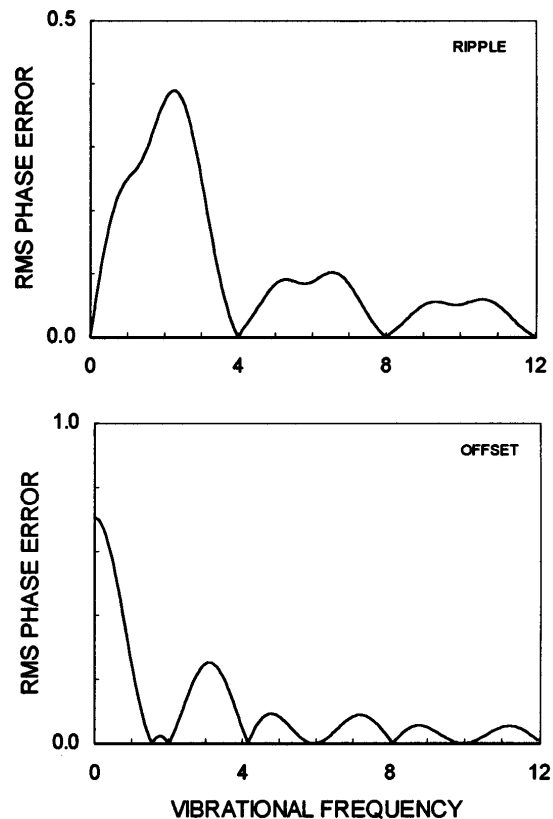


Fig. 5. Predicted rms phase-measurement errors for the three-bucket algorithm calculated with an integrating bucket of length $\beta = \pi/2$. The gradual decline in sensitivity with higher frequency is due to the smoothing effect of the integrating bucket.

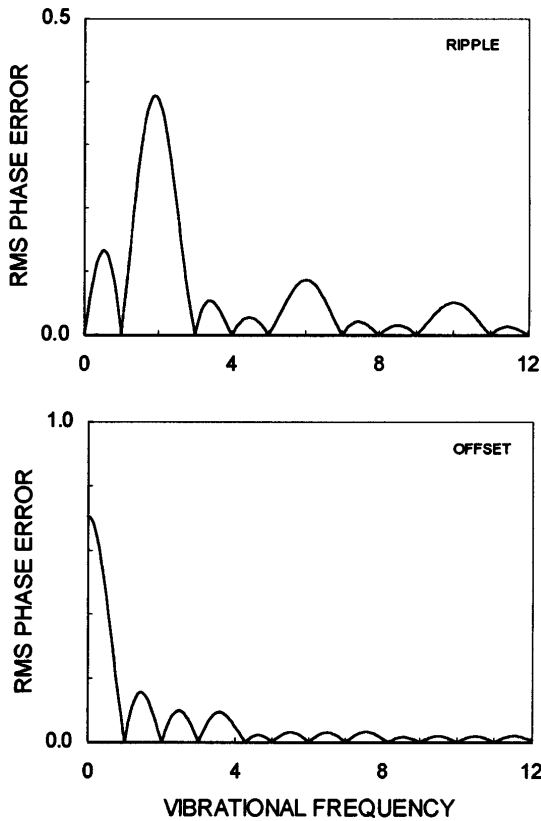


Fig. 6. Predicted rms phase-measurement errors for the four-bucket algorithm calculated with an integrating bucket of length $\beta = \pi/2$.

where

$$c(\nu, \theta, \alpha) = \text{Re}[P_0(\nu)\exp(i\alpha)], \tag{72}$$

$$r(\nu, \theta, \alpha) = \text{Re}[P_1(\nu)\exp(i\alpha)]\cos(2\theta) + \text{Re}[P_2(\nu)\exp(i\alpha)]\sin(2\theta). \tag{73}$$

Separating out the phase-independent terms and integrating over the angles θ and α reduces these equations to the relatively simple forms

$$C(\nu) = 1/\sqrt{2} |P_0(\nu)|, \tag{74}$$

$$R(\nu) = 1/2 |P_1(\nu) + P_2(\nu)|, \tag{75}$$

where for Eq. (75) we have made use of the orthogonality of the functions $P_1(\nu)$ and $P_2(\nu)$ to simplify $R(\nu)$.²³ Thus the rms error in the presence of a vibration of random phase is a simple function of the previously derived coefficients of the phase-error transfer function $P(\nu, \theta)$.

It is asserted here without rigorous proof that in many cases one can calculate the net mean-square error for a vibration composed of multiple frequencies simply by summing the mean-square errors for the various frequency components of the spectrum. This is a safe assumption for vibrations resulting from a few, well-separated frequencies. In that case we can express the net errors as a function of a discrete power spectrum A_ν :²

$$E_{\text{NET}}^{(c)} = \left[\sum_{\nu} A_{\nu}^2 C(\nu)^2 \right]^{1/2}, \tag{76}$$

$$E_{\text{NET}}^{(r)} = \left[\sum_{\nu} A_{\nu}^2 R(\nu)^2 \right]^{1/2}. \tag{77}$$

These equations should be used with caution, however, because there can be situations in which multiple vibrations having a common source are correlated in phase. Such a correlation would prohibit a calculation based on the power spectrum alone.

8. SPECTRA OF VIBRATION SENSITIVITY

The formulas for $C(\nu)$ and $R(\nu)$ result in relatively simple analytical formulas for predicting the effect of vibrations of various frequencies. For example, from Eqs. (57), (74), and (75), the five-bucket algorithm has a predicted rms ripple of

$$R(\nu) = \left[\frac{B_{\nu+1}^2 + B_{\nu-1}^2}{2} \right]^{1/2} \left| \frac{\cos(\nu\pi/2)\sin^2(\nu\pi/4)}{2} \right|. \tag{78}$$

Figures 4–9 show the phase error in radians of the various PSI algorithms considered in Section 3 for pure vibrational tones, calculated from the corresponding phase-error transfer functions together with Eqs. (74) and (75).

A number of important conclusions may be drawn from the general appearance of the vibration-sensitivity spectra in the figures. First, all the plots show a prominent peak near a vibrational frequency of $\nu = 2$, corresponding to two mechanical oscillations during a $\phi = 2\pi$ phase shift. The reason for this sensitivity is that a $\nu = 2$ vibration generates intensity distortions at two frequencies, $\hat{\nu} = 1$ and $\hat{\nu} = 3$. An intensity distortion at $\hat{\nu} = 1$ is indistinguishable from real fringe data, which have exactly

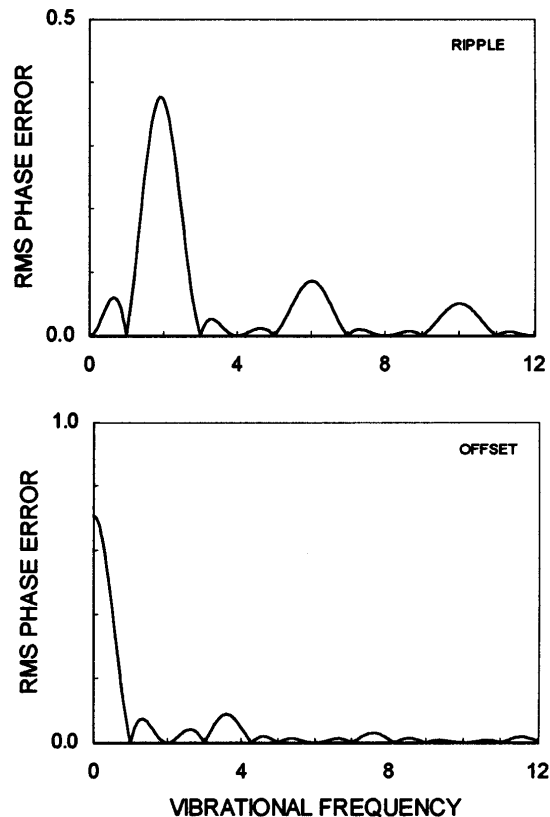


Fig. 7. Predicted rms phase-measurement errors for the Schwider–Hariharan five-bucket algorithm calculated with an integrating bucket of length $\beta = \pi/2$.

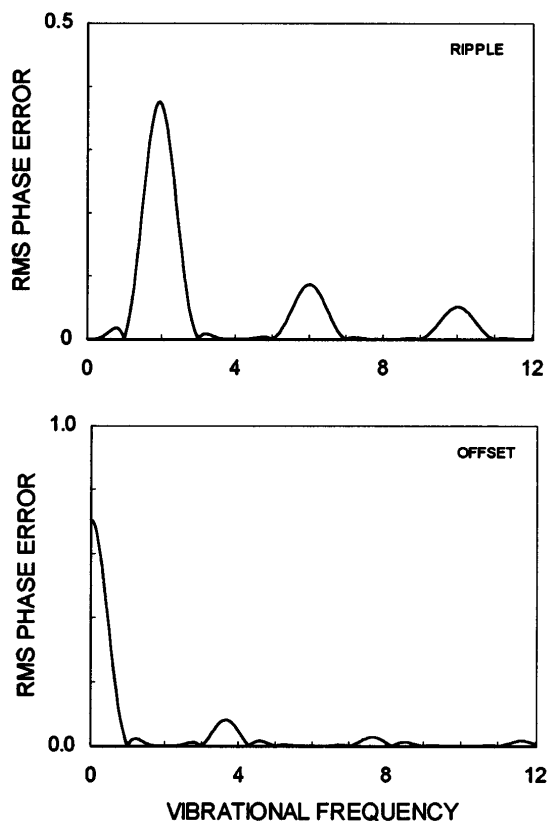


Fig. 8. Predicted rms phase-measurement errors for the seven-bucket algorithm calculated with an integrating bucket of length $\beta = \pi/2$. This algorithm has the lowest overall sensitivity to vibration, particularly in the low-frequency region ($\nu < 1$).

the same frequency. Consequently the number of buckets or the particular sampling weights used is not that important. In fact, when averaged over all vibrational phase angles α , all the algorithms have exactly the same sensitivity to vibration at $\nu = 2$. A vibration of 100-nm amplitude at a frequency of $\nu = 2$ will typically generate rms measurement errors of 40 nm.

Another general observation that can be made is that the sensitivity to vibration decreases with vibrational frequency, primarily because of the smoothing effect of the integrating bucket. Without this integration the sensitivity to vibration remains strong even at very high frequencies because of the aliasing effect of the sparse data sampling (Fig. 4). The integrating-bucket technique does more for the reduction of vibration than does any other aspect of the PSI measurement method.

What does change significantly from algorithm to algorithm is the sensitivity to frequencies other than $\nu = 2$. The four-bucket algorithm (Fig. 6) is clearly better than the three-bucket algorithm (Fig. 5), whereas the Larkin–Oreb approach (Fig. 9) has a different distribution of peaks that may prove advantageous for some environments. The seven-bucket algorithm (Fig. 8) is relatively insensitive to low-frequency vibrations ($\nu < 1$), as has been verified in the experimental work described in Section 9.

The $C(\nu)$ or constant term is normally considered to be unimportant because it is the same for all the points or pixels in the interference pattern, provided, of course, that all the points are measured simultaneously. It may,

however, be important to note that this idealization is not realized in practice. Common CCD video cameras do not take instantaneous snapshots of an image but instead integrate data progressively across the field. This method leads to a time lag between the first and the last pixel that can result in corruption or distortion of the final phase image because of a time-varying phase offset. This distortion would not appear as the familiar phase ripple that correlates to the fringe pattern but would be a much more subtle, quasi-sinusoidal, field-dependent error.

9. EXPERIMENT

A suitable apparatus for experimental verification of the theoretical method is shown in Fig. 10. Two different PZT translators control the position of the objective in an interference microscope. The first PZT provides the conventional phase-shift ramp, whereas the second introduces additional motion that mimics the effects of mechanical vibration. The waveform generator in the figure determines the frequency and the amplitude of the vibration. The camera acquires data at 25 Hz, so the ramp covers 2π rad of interference phase 6.25 times/s. For this camera a vibrational frequency of 6.25 Hz is therefore normalized to 1.

Figure 11 shows the experimentally determined sensitivity of the interferometer to vibration as a function of frequency when the five-bucket algorithm is used. Given the small size of the errors and the difficulty of isolating the various error sources, the agreement is quite good. We can see all the important characteristics of

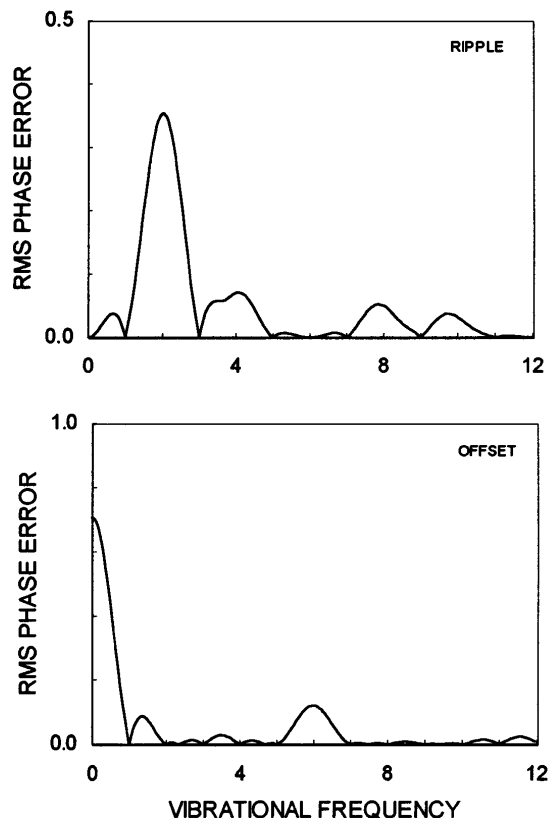


Fig. 9. Predicted rms phase-measurement errors for the Larkin–Oreb algorithm, calculated with an integrating bucket of length $\beta = \pi/3$. The peak sensitivities above $\nu = 3$ are not the same as for algorithms based on $\pi/2$ phase shifts.

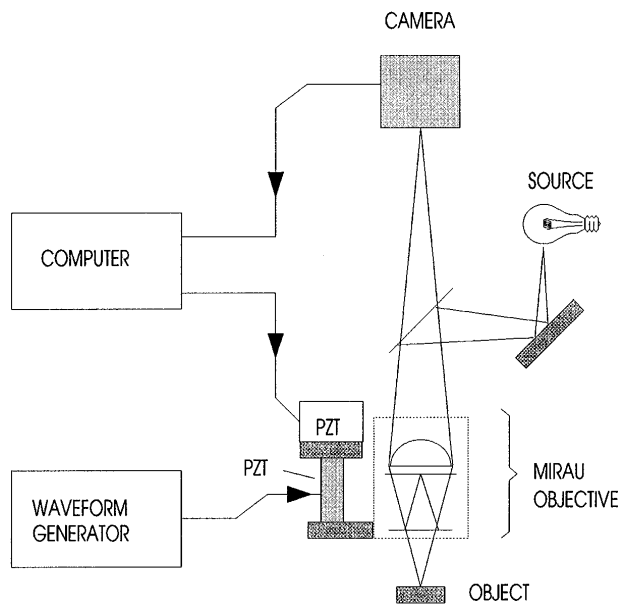


Fig. 10. Experimental system for introducing controlled amounts of vibrational noise. The system is a conventional interferometric microscope with an additional PZT driven by a sinusoidal waveform generator.

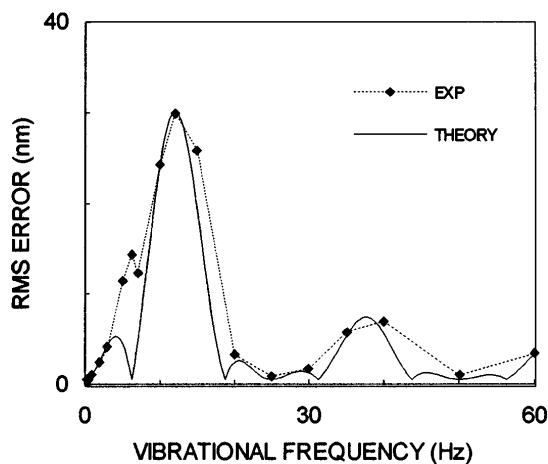


Fig. 11. Comparison of theoretical and experimental sensitivity of the five-bucket algorithm with vibration as a function of frequency, for a vibrational amplitude of one-quarter fringe. These data were obtained with the apparatus shown in Fig. 10.

the sensitivity, including the expected peaks at 12.5 and 45 Hz. The major discrepancy is near the first minimum at 6.25 Hz, which is much larger than that predicted by theory. This is due to the large amplitude of the vibration (one-quarter fringe).

10. CONCLUSIONS

A generally acknowledged drawback of phase-shifting interferometry is its sensitivity to vibration. The present study both confirms and qualifies this assertion. It is true that for most common forms of PSI there are certain vibrational frequencies that will invariably introduce errors, and the best insurance against these errors is mechanical isolation. However, if the frequency spectrum of the vibration is reasonably well defined, it is often pos-

sible to perform accurate PSI without complete mechanical isolation.

The purpose of this study therefore is to assist in quantifying the effects of vibration and perhaps to provide a means of dealing with these effects without expensive hardware modifications. The principal mathematical results are contained in Eqs. (32) and (33), which are formulas for calculating the net effect of a vibration given its complex spectrum, and in Eqs. (74) and (75), which are formulas for estimating typical rms instrument performance in the presence of uncorrelated vibrations of random phase.

These results may be used in a variety of ways. One possibility is to use the results of this study in the comparison of the overall vibrational noise spectrum with the vibrational sensitivity of an interferometer setup. Sometimes it is possible to adjust the data-acquisition rate of the interferometer to shift the peak vibrational sensitivity away from a known source of vibration. This does not necessarily mean increasing the speed of data acquisition. If the vibration has a fairly narrow high-frequency spectrum, it may be advantageous to slow the data acquisition down to bring the vibrational frequency into a region of zero sensitivity.

If the vibration is confined to the low-frequency region, there is progressively better performance with the three-, four-, five-, and seven-bucket algorithms. The improvement in performance is much greater than might be expected from a simple statistical argument based on the number of buckets. The three-bucket algorithm is several orders of magnitude more sensitive to low-frequency vibrations than is the seven-bucket algorithm. Examples of low-frequency vibration include thermal distortions, floor motion, and some of the most common forms of environmental noise.

As a final example, I present in Fig. 12 the results of using the seven-bucket algorithm under conditions identical to those used in generating the phase-error map shown in Fig. 1. The periodic error is eliminated, even though the instrument and the environment are identical. Although this improvement is restricted to a fairly narrow frequency band, it does serve to illustrate that one can do

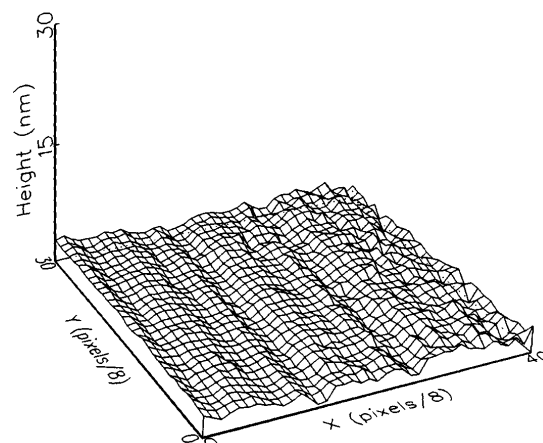


Fig. 12. Experimental demonstration of the improvement in performance when the seven-bucket algorithm is used. This is the phase-error map for an interferometer in the presence of the same 1-Hz vibration used when generating Fig. 1. The periodic error is suppressed, as predicted by the theory.

much to improve PSI performance without substantially changing the hardware.

ACKNOWLEDGMENTS

A paper of this length and mathematical detail is difficult to write, but it is even more difficult to review. I had the very good fortune of having H. M. Martin of the Steward Observatory as reviewer. His careful and detailed analysis of the original manuscript significantly improved the quality and the consistency of the mathematical treatment, and I gratefully acknowledge his assistance.

REFERENCES AND NOTES

1. J. E. Greivenkamp and J. H. Bruning, "Phase shifting interferometry," in *Optical Shop Testing*, D. Malacara, ed. (Wiley, New York, 1992), Chap. 14.
2. P. Hariharan, *Optical Interferometry* (Academic, Orlando, Fla., 1985).
3. Y. Y. Cheng and J. C. Wyant, "Phase shifter calibration in phase-shifting interferometry," *Appl. Opt.* **24**, 3049–3052 (1985).
4. Y. Y. Cheng and J. C. Wyant, "Effect of piezoelectric transducer nonlinearity on phase shift interferometry," *Appl. Opt.* **26**, 1112–1116 (1987).
5. C. P. Brophy, "Effect of intensity error correlation on the computed phase of phase-shifting interferometry," *J. Opt. Soc. Am. A* **7**, 537–541 (1990).
6. C. Ai and J. C. Wyant, "Effect of spurious reflection on phase shift interferometry," *Appl. Opt.* **27**, 3039–3045 (1988).
7. P. Hariharan, "Digital phase-stepping interferometry: effects of multiply reflected beams," *Appl. Opt.* **26**, 2506–2507 (1987).
8. K. Creath, "Comparison of phase-measurement algorithms," in *Surface Characterization and Testing*, K. Creath, ed., *Proc. Soc. Photo-Opt. Instrum. Eng.* **680**, 19–28 (1986).
9. J. van Wingerden, H. H. Frankena, and C. Smorenburg, "Linear approximation for measurement errors in phase shifting interferometry," *Appl. Opt.* **30**, 2718–2729 (1991).
10. K. Kinnstätter, Q. W. Lohmann, J. Schwider, and N. Streibl, "Accuracy of phase shifting interferometry," *Appl. Opt.* **27**, 5082–5089 (1988).
11. K. Freischlad and C. L. Koliopoulos, "Fourier description of digital phase-measuring interferometry," *J. Opt. Soc. Am. A* **7**, 542–551 (1990).
12. J. H. Bruning, D. R. Herriott, J. E. Gallagher, D. P. Rosenfeld, A. D. White, and D. J. Brangaccio, "Digital wavefront measuring interferometer for testing optical surfaces and lenses," *Appl. Opt.* **13**, 2693–2703 (1974).
13. K. G. Larkin and B. F. Oreb, "Design and assessment of symmetrical phase-shifting algorithms," *J. Opt. Soc. Am. A* **9**, 1740–1748 (1992).
14. G. Arfken, *Mathematical Methods for Physicists*, 2nd ed. (Academic, New York, 1970), p. 682.
15. J. C. Wyant, C. L. Koliopoulos, B. Bushan, and O. E. George, "An optical profilometer for surface characterization of magnetic media," *ASLE Trans.* **27**, 101–107 (1984).
16. J. C. Wyant, "Interferometric optical metrology: basic principles and new systems," *Laser Focus* (May 1982), pp. 65–71.
17. J. Schwider, R. Burow, K.-E. Elssner, J. Grzanna, R. Spolaczyk, and K. Merkel, "Digital wave-front measuring interferometry: some systematic error sources," *Appl. Opt.* **22**, 3421–3432 (1983).
18. P. Hariharan, B. F. Oreb, and T. Eiju, "Digital phase-shifting interferometry: a simple error-compensating phase calculation algorithm," *Appl. Opt.* **26**, 2504–2506 (1987).
19. J. E. Greivenkamp and J. H. Bruning, "Phase shifting interferometry," in *Optical Shop Testing*, D. Malacara, ed. (Wiley, New York, 1992).
20. P. de Groot, "Derivation of algorithms for phase-shifting interferometry using the concept of a data sampling window," *Appl. Opt.* (to be published).
21. P. de Groot, "Long-wavelength laser diode interferometer for surface flatness measurement," in *Optical Measurements and Sensors for the Process Industries*, C. Gorecki and R. Preator, eds., *Proc. Soc. Photo-Opt. Instrum. Eng.* **2248**, 136–140 (1994).
22. K. G. Larkin and B. F. Oreb, "A new seven-sample symmetrical phase-shifting algorithm," in *Interferometry: Techniques and Analysis*, G. M. Brown, M. Kujawinska, O. Y. Kwon, G. T. Reid, eds., *Proc. Soc. Photo-Opt. Instrum. Eng.* **1755**, 2–11 (1992).
23. The orthogonality of the functions $P_1(\nu)$, $P_2(\nu)$ in phase space is obvious for symmetric sampling functions because in this case $P_1(\nu)$ is purely real and $P_2(\nu)$ purely imaginary. The orthogonality of these functions for asymmetric sampling functions follows from the observation that the effect of asymmetry in common PSI algorithms can be reduced to a simultaneous phase shift of both $P_1(\nu)$ and $P_2(\nu)$.

Vibration in phase-shifting interferometry: errata

Peter J. de Groot

Zygo Corporation, Laurel Brook Road, Middlefield, Connecticut 06455

I would like to correct errors that appeared in two equations published in Ref. 1.

Equation (38) should read

$$B(\hat{\nu}) = \frac{\sin(\hat{\nu}\beta/2)}{\hat{\nu} \sin(\beta/2)}, \quad (38)$$

and Eq. (48) should read

$$\begin{aligned} P_0(\nu) &= \frac{\exp(i3\nu\pi/4)\cos(\nu\pi/4)}{2} [(B_{\nu+1} + B_{\nu-1}) \\ &\quad \times \cos(\nu\pi/4) + (B_{\nu+1} - B_{\nu-1})\sin(\nu\pi/4)] \\ P_1(\nu) &= \frac{i \exp(i3\nu\pi/4)\sin(\nu\pi/4)}{2} [(B_{\nu+1} + B_{\nu-1}) \\ &\quad \times \cos(\nu\pi/4) + (B_{\nu+1} - B_{\nu-1})\sin(\nu\pi/4)] \\ P_2(\nu) &= -\frac{\exp(i3\nu\pi/4)\sin(\nu\pi/4)}{2} [(B_{\nu+1} - B_{\nu-1}) \\ &\quad \times \cos(\nu\pi/4) + (B_{\nu+1} + B_{\nu-1})\sin(\nu\pi/4)]. \end{aligned} \quad (48)$$

REFERENCE

1. P. J. de Groot, "Vibration in phase-shifting interferometry," *J. Opt. Soc. Am. A* **12**, 354–365 (1995).